Journal of Materials Chemistry A

ROYAL SOCIETY OF CHEMISTRY

PAPER

View Article Online
View Journal

Cite this: DOI: 10.1039/d5ta09730d

Interface-engineered melt-spun BiSbTe for multiscale phonon scattering and enhanced thermoelectric performance

Yae Eun Park,†[a] Hyunjin Han,†[a] Sung-Jin Jung,†[b] Junwoo Song,[b] Jino Kim,[b] Jungwon Na,[b] Kwangjoo Kim,[b] Insub Lee,[b] Hoon Wee,[b] Joonhyun Lee,[b] Sungjun Yang,[c] Seungki Jo,[d] Ho Seong Lee,[e] Tae Joo Shin,[f] Youngdeog Koh *[b] and Jae Sung Son *[a]

Thermoelectric materials have attracted tremendous attention owing to their ability to directly convert heat into electricity. Enhancing the thermoelectric efficiency of materials relies on minimizing thermal conductivity *via* phonon scattering engineering, where the broad spectrum of phonon frequencies requires multiscale architectures capable of scattering phonons over diverse wavelengths. In this study, we developed BiSbTe-based thermoelectric materials featuring multiscale hierarchical microstructures, achieved *via* melt-spinning synthesis of nanostructured BiSbTe particles followed by solution-phase coating with polyoxometalates (POMs). During spark plasma sintering, the POM surface layers decompose to form ultrathin oxide interfacial layers within the BiSbTe grains. These oxide interfaces, in combination with nanoscale features, effectively suppress lattice thermal conductivity to 0.38 W m^{-1} K^{-1} at room temperature with only 0.1 mol% POM additive, yielding a peak figure of merit (*ZT*) of 1.56 at 75 °C. This work demonstrates a scalable strategy for realizing multiscale phonon scattering and enhanced thermoelectric performance through interface engineering.

Received 28th November 2025
Accepted 31st March 2026

DOI: 10.1039/d5ta09730d

rsc.li/materials-a

Introduction

Thermoelectric (TE) materials, which enable direct conversion between heat and electricity, hold great promise for energy harvesting and solid-state cooling applications.[1–6] Despite these advantages, broad deployment of TE systems has still been constrained by low conversion efficiency, which is governed by the dimensionless figure of merit, $ZT = \sigma S^2 T/\kappa$, where S represents the Seebeck coefficient, σ is the electrical conductivity, T is the absolute temperature, and κ is the total thermal conductivity. Enhancing ZT requires increasing the power factor (σS^2) while simultaneously lowering thermal conductivity. However, these transport parameters are typically interdependent, making concurrent optimization challenging.

So far, for enhancing ZT values, a wide range of approaches have been developed to suppress lattice thermal conductivity by engineering phonon scattering. Classical strategies include introducing heavy elements[7] and weak interatomic bonds[8–10] to lower phonon velocities, exploiting strong lattice anharmonicity[11,12] or complex unit cells[5,13] to enhance phonon–phonon interactions, and utilizing alloying,[14,15] nanostructuring,[16–19] and defect engineering[20,21] to create additional phonon scattering centers. Since phonons span a wide wavelength spectrum, a single strategy is often insufficient to minimize lattice thermal conductivity.[22,23] To effectively suppress lattice thermal conductivity, phonon scattering mechanisms can be tailored across multiple wavelength regimes. While high-frequency phonons are predominantly scattered by atomic-scale disorders such as mass disorder in alloys and point defects, which mainly arise from mass and strain fluctuations, medium-and low-frequency phonons are generally scattered by microstructural features. For example, nanostructuring approaches, such as nanoprecipitates, nanopores, and inclusions, have been intensively studied for suppressing mid-frequency phonons, thereby enhancing ZT values. Another strategy to suppress mid- and low-frequency phonons has been interface engineering including grain boundary engineering or the introduction of heterogeneous interfacial layers. To achieve ultralow thermal conductivity, multiscale structures are therefore required to

[a]Department of Chemical Engineering, Pohang University of Science and Technology, Pohang, Republic of Korea. E-mail: sonjs@postech.ac.kr
[b]Samsung Research, Samsung Electronics, Seoul, Republic of Korea
[c]Office of Research Facilities and Training (ResFacT), Ulsan National Institute of Science and Technology (UNIST), Ulsan, Republic of Korea
[d]Nano Materials Research Division, Korea Institute of Materials Science (KIMS), Changwon, Republic of Korea
[e]Department of Materials Science and Metallurgical Engineering, Kyungpook National University, Daegu, Republic of Korea
[f]School of Semiconductor Materials and Devices Engineering, Ulsan National Institute of Science and Technology (UNIST), Ulsan, Republic of Korea
† These authors contributed equally.

hierarchically scatter phonons across the full wavelength spectrum.

Polyoxometalates (POMs)—a family of sub-nanometer molecular clusters composed of transition metals (Mo, W, V) and oxygen atoms together with central heteroatoms (*e.g.*, P, Si, Sb)—can offer intriguing candidates as additives for phonon engineering of TE materials. POMs offer remarkable structural and electronic tunability, enabling control over redox states, electron storage, and interfacial properties. Although widely investigated in catalysis, energy storage, and molecular electronics, research on POMs for thermoelectrics remains insufficient. Their distinct attributes, however, suggest a role: they can form interfacial phases like oxides that introduce significant mass contrast, lattice distortions, and structural complexity, thereby serving as effective phonon scatterers. Also, they can modulate carrier concentration or introduce carrier-trapping sites, additional sources for modulating electrical properties for TE materials. In this work, we report efficient BiSbTe TE materials with multiscale microstructures to hierarchically scatter phonons. First, nanostructuring *via* a melt spinning process for the synthesis of BiSbTe generates ultrafine grains, dense defects, and nanocrystalline regions, which efficiently scatter short- to mid-wavelength phonons. Second, we introduce POM layers on the surface of melt-spun Bi–Sb–Te particles, which leads to the formation of POM-derived interfacial oxides during spark plasma sintering (SPS) that are highly effective in scattering mid- to long-wavelength phonons. These multiscale structures enable hierarchical phonon scattering across the entire phonon spectrum, leading to a substantial reduction in lattice thermal conductivity—down to approximately 0.38 W m^{-1} K^{-1} at room temperature with only 0.1 mol% POM loading. This significant suppression of thermal conductivity allows our Bi–Sb–Te nanocomposites to achieve a maximum *ZT* value of 1.56 at 75 °C, demonstrating the potential of POMs as phonon-engineered additives for high-performance TE applications.

Results and discussion

$Bi_{0.5}Sb_{1.5}Te_3$ particles were synthesized by melt spinning, subsequently coated with a POM layer, and consolidated by SPS to yield *x* mol% POM coated BiSbTe particles ($x = 0, 0.1, 0.3, 0.5$) (Fig. 1a). The thickness of melt-spun ribbons ranges from 80 to

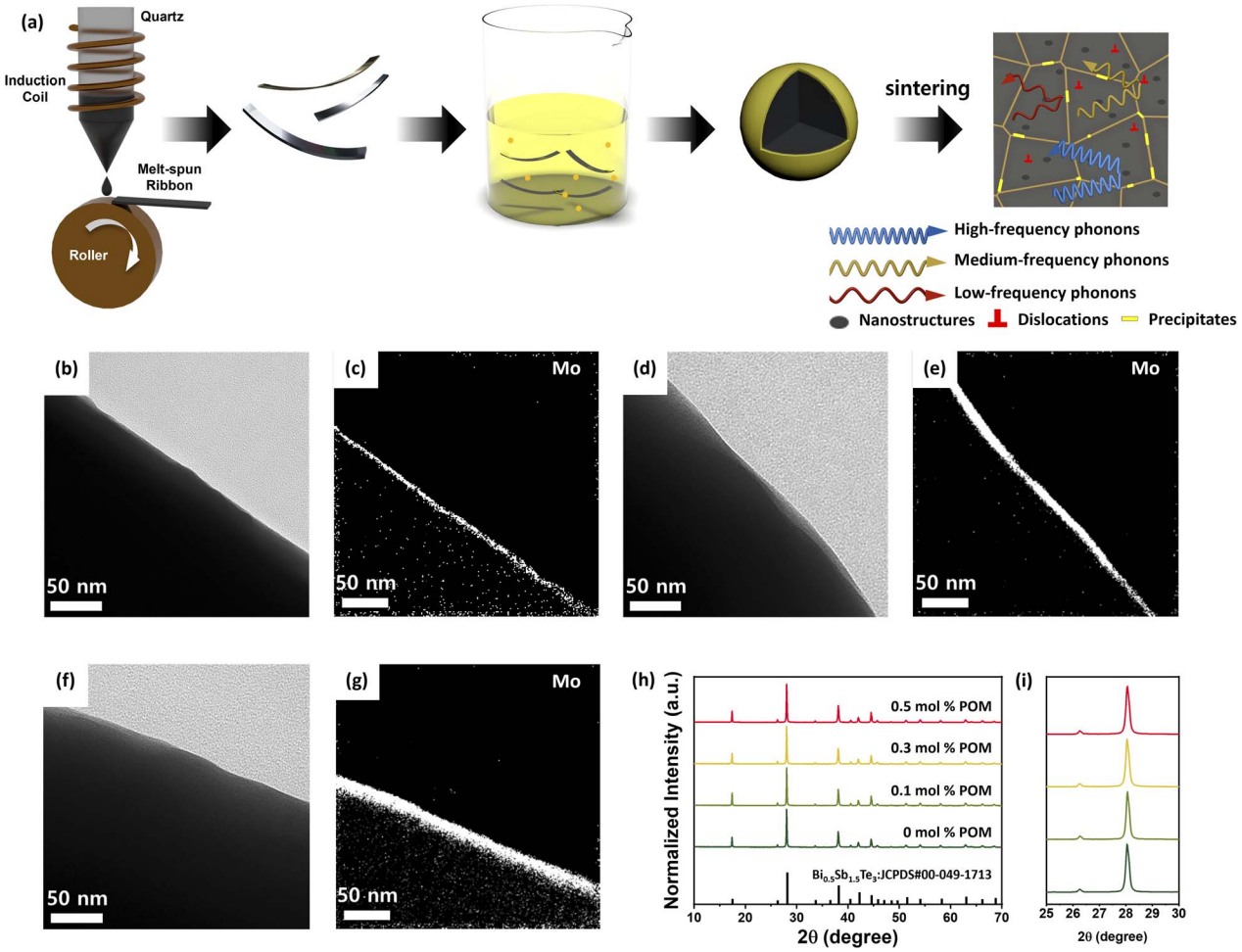

Fig. 1 (a) Schematic diagram of the overall process. TEM and EELS images for POM contents of (b and c) 0.1 mol%, (d and e) 0.3 mol% and (f and g) 0.5 mol%. EELS mapping was performed for Mo within the POM molecules. (h) XRD patterns of TE powders with POM contents and (i) enlarged XRD patterns in the 2θ range of 25–30°.

120 μm, and the crystal size estimated by scanning electron microscopy (SEM) analysis was 1–10 μm (Fig. S1). Typically, as-synthesized BiSbTe powder was dispersed and stirred in the solution of $(NH_4)_3PO_4 12MoO_3 \cdot xH_2O$ (POM molecules). The median size of the melt-spun, stirred powder estimated by laser diffraction was 7.67 μm (Fig. S2). This indicates that the melt-spun ribbons were fragmented into smaller particles during stirring. Upon stirring, the yellow color of the POM in the solution turned transparent (Fig. S3), suggesting that POM anions were coated on the surface of BiSbTe particles. The SEM images (Fig. S4) show elongated particles with sizes ranging from several to several tens of micrometers. The elongated morphology can be attributed to the nature of the melt spinning synthesis process to produce ribbon-like powders. Transmission electron microscopy (TEM) and electron energy loss spectroscopy (EELS) images (Fig. 1b–g) reveal that P and Mo elements were exclusively detected only at the surface of BiSbTe particles as uniform thin films, indicating the effective coating of POM on the surfaces. Moreover, with increasing POM loading, the thickness of the POM layer gradually increased, *e.g.* at 0.1 mol%, POM formed an ~5 nm thick layer, which increased to ~13 nm at 0.3 mol% and ~20 nm at 0.5 mol% (Fig. 1c, e and g). Powder X-ray diffraction (XRD) patterns for all particles show only peaks assignable to the rhombohedral BiSbTe phase without second-phase peaks (Fig. 1h). Also, any peak shift resulting from the reaction between the POM and BiSbTe was not observed in the XRD patterns (Fig. 1i), suggesting the physical adsorption of the POM on the surface of BiSbTe.

The POM-coated BiSbTe powder was sintered by SPS at 450 °C under 45 MPa, producing dense pellets with relative densities 95.3–97.5% of the theoretical density, indicating near-full densification with minimal residual porosity. The XRD patterns of the sintered samples show peaks corresponding to the rhombohedral BiSbTe phase without second-phase peaks, indicating that the content of the created phase from the POM was below the detection threshold (Fig. 2a). However, as the POM content increased, the XRD peaks were shifted to lower angles, suggesting evolution toward a Bi-rich and Sb-deficient phase (Fig. 2b). To quantify this shift, the lattice parameters were further analyzed. In this work, however, we focused on quantifying lattice-parameter changes from peak positions across samples by the Le Bail fitting method (Fig. S5 and S6).[24] Using the XRD data, Le Bail refinement reveals a clear, concentration-dependent lattice expansion after sintering. The lattice parameters remain nearly unchanged at 0–0.1% POM, whereas both lattice constants of *a* and *c* increase noticeably for ≥0.3 mol% POM, consistent with the systematic low-angle peak shift. This change in the lattice constant can be attributed to Sb-oxide formation.

To further understand the formation of the interfacial phase from the POM layer, the POM was analyzed by thermogravimetric analysis (TGA). POM molecules are known to form various oxides upon heating through solid-state thermal decomposition.[25] The TGA spectrum shows two weight losses: one at a low temperature of ~80 °C and another at a high temperature of 390–450 °C (Fig. S7), agreeing with a previous report.[26] While the former weight loss is attributable to dehydration from the $(NH_4)_3PO_4 12MoO_3 \cdot xH_2O$ of the POM molecule, the latter can be the loss of gaseous NH_3 from the counter balance cation of NH_4 of POM anions. Moreover, the heat-treated POM at 450 °C corresponding to the sintering temperature (Fig. S8a) shows definite peaks in the XRD patterns, indicating the formation of crystalline oxide phases by thermal decomposition. Also, the characteristic yellow color of POM molecules was transformed to blue-black upon heating (Fig. S8b), agreeing with those of the hydrogen molybdenum phosphate or molybdenum phosphate phases in the previous report.[27] These results suggest the formation of interfacial oxide layers among BiSbTe grains.

Scanning electron microscopy (SEM) images of the POM-BiSbTe samples show well-sintered grains (Fig. 2c, d and S9a–

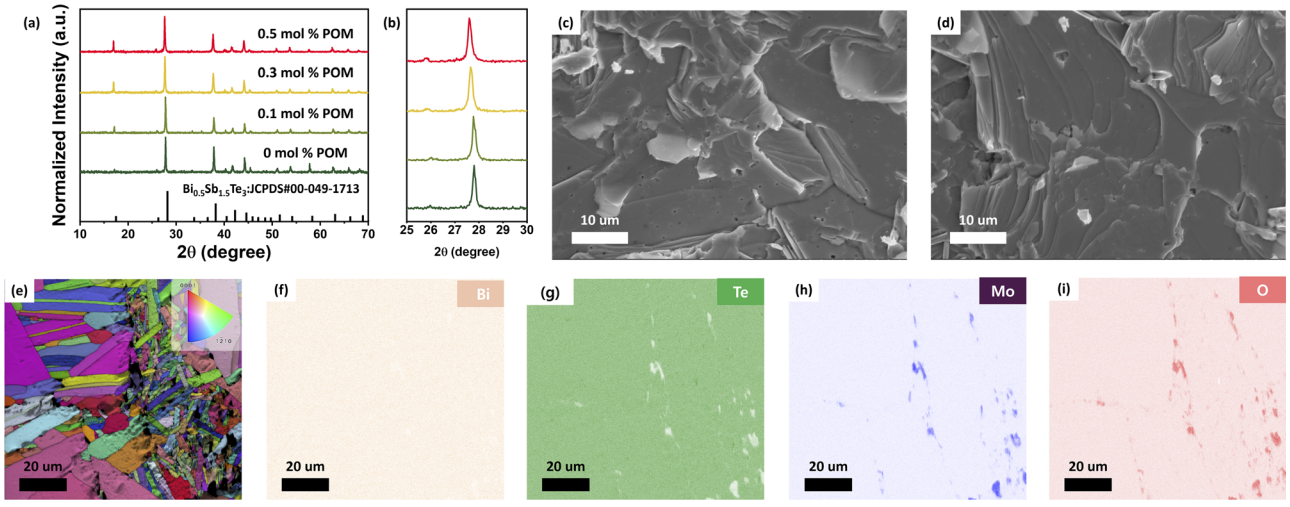

Fig. 2 (a) XRD patterns of SPS-ed TE samples with varying POM contents and (b) enlarged XRD patterns in the 2θ range of 25–30°. SEM images of the fractured in-plane surface showing the microstructures of (c) 0 mol% and (d) 0.1 mol% POM-coated BiSbTe. (e) EBSD of 0.1 mol% POM-coated BiSbTe and EDS mapping images of (f) Bi, (g) Te, (h) Mo, and (i) O elements.

d) and no remarkable changes in microstructures were observed in the samples with the POM layers. Fig. S9e–h exhibit stacked layered structures characteristic of BiSbTe's van der Waals crystal structures, with basal planes preferentially aligned parallel to the pressing direction (*c*-axis perpendicular to layers), demonstrating crystallographic texture development during SPS. To further confirm the crystalline orientation of SPS-ed samples, the XRD analysis was conducted for the sample in in-plane and through-plane directions (Fig. S10). As expected, the XRD patterns displayed stronger *c*-axis peaks indexed to (006), (009), (0015), and (0018) crystalline planes in the pattern obtained in the in-plane direction, while the corresponding peaks in the through-plane direction exhibit significantly reduced intensities.

To confirm the formation of oxide layers, electron backscatter diffraction (EBSD) analysis was further carried out. Fig. 2e presents the image quality (IQ) map together with the inverse pole figure (IPF) map. The IQ map was employed to assess the local crystal quality based on the sharpness of the EBSD patterns,[28] while the IPF map was used to visualize the crystallographic orientation of each grain by representing the crystal direction parallel to the sample normal with different colors.[29] The EBSD image shows microstructural characteristics of typical polycrystalline crystals and a wide range of grain sizes from several hundred nanometers to several tens of micrometers. These diverse grain sizes are beneficial to scatter phonons across a wide spectrum of wavelengths. In addition, it exhibited pronounced color diversity, suggesting large orientation fluctuations among adjacent grains. Since each color represents a distinct crystallographic orientation, such strong color contrast indicates orientation variations. In the energy dispersive spectroscopy (EDS) mapping images (Fig. 2f–i), Mo and O elements were exclusively detected between BiSbTe grains and the layer thickness ranged from several tens of nanometers to several micrometers, confirming the formation of oxide interfacial layers.

To further understand the interfacial oxide layers created in BiSbTe grains, we investigated the microstructures by TEM analysis. As shown in Fig. 3a and S11, a variety of nanostructures with sizes ranging from a few to several tens of nanometers were observed, which originated from the melt-spinning and SPS processes.[30] Additionally, Moiré patterns up to approximately 65 nm wide were identified at the grain boundaries (Fig. 3b). The observed Moiré patterns suggest that the grains exhibit high crystallinity and possess clean grain boundaries.[31] Scanning transmission electron microscopy (STEM) images (Fig. 3c and d) reveal the presence of precipitates distributed along the grain boundaries of the BiSbTe matrix, with sizes ranging from several tens to several hundreds of nanometers. EDS analysis confirmed two distinct types of precipitates of Sb-rich oxide phases and Mo-rich oxide phases (Fig. S12), indicating the formation of interfacial oxide layers from the reaction between POM and BiSbTe. These secondary phases introduce mass and strain field fluctuations, acting as additional phonon scattering centers. Moreover, inside the grain, a large number of dislocations were observed clearly. Fig. 3e presents an enlarged image of the grain interior shown in Fig. 3c, where dense dislocations can be identified in the inverse fast Fourier transform (IFFT) image (Fig. 3f).

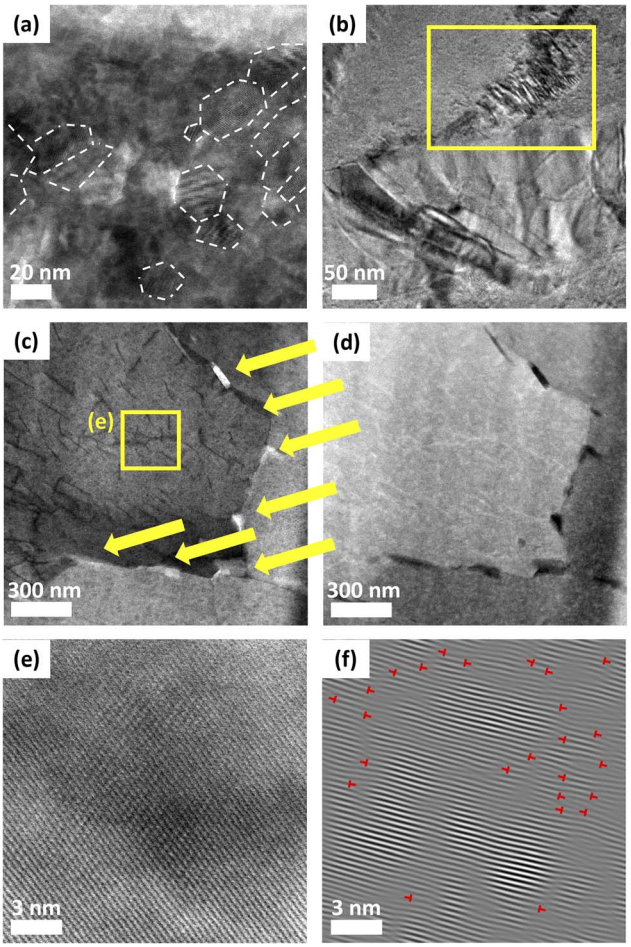

Fig. 3 Microstructures of the 0.1 mol% POM-coated sample. HRTEM images of (a) nanostructures and (b) Moiré patterns. (c) Bright field (BF) and (d) high-angle annular dark-field (HAADF) STEM images of grain boundaries. The yellow arrows indicate oxide precipitates. (e) Enlarged view of the boxed region in (c). (f) IFFT image of (e).

To understand the microstructural changes by the POM addition, we conducted TEM analysis on the sample without POM addition. Interestingly, various nanostructures were clearly observed, while no distinct dislocations were identified in the sample without POM addition, implying a low dislocation density. As the POM-added exhibited a significantly higher dislocation density, this result implies that the POM addition plays a critical role in generating dislocation defects.

In general, dislocation nucleation can be promoted by local stress concentration associated with defects, precipitates, thermal-expansion mismatch, or chemical heterogeneity developed during processing.[32–34] We interpret the high dislocation density observed in the POM-added sample as arising from the combination of the layered structural nature of Bi_2Te_3-based materials and the additional internal stress introduced by POM addition. In Bi_2Te_3-type layered compounds, the weak van der Waals bonding between quintuple layers reduces the

resistance to interlayer sliding along the basal plane, which can make dislocation formation more favorable.[35]

The multiscale microstructural design—comprising mass fluctuation induced by POM incorporation and melt spinning, nanostructures ranging from a few to several tens of nanometers, interfacial oxides tens to hundreds of nanometers in size, and a wide grain size distribution (from several hundred nanometers to tens of micrometers)—collectively facilitates efficient phonon scattering over a broad range of wavelengths. Consequently, the hierarchical structure effectively suppresses lattice thermal conductivity by targeting phonons with frequency ranging from low- to high-frequency.

Temperature-dependent electrical and thermal transport properties of all four samples are displayed in Fig. 4 and 5. All measurements were performed in the direction parallel to the pressing axis during SPS. The thermoelectric properties measured along the perpendicular direction are presented in Fig. S13. The general dependence of thermoelectric properties on the POM content is consistent with that observed in the parallel direction, although the *ZT* values are slightly lower. Accordingly, here, we focus on the properties measured in the parallel direction.

To understand the effect of the POM interlayer on the electrical properties, we performed Hall measurements on four samples with POM contents of 0, 0.1, 0.3, and 0.5 mol%. With increasing POM content, hole concentrations gradually decreased from 2.12×10^{19} cm^{-3} to 1.78×10^{19} cm^{-3} (Fig. 4a). This reduction in hole concentration is in line with the XRD peak shift indicating an Sb-deficient phase as Sb_{Te} antisite defects serve as hole-donating defects in the BiSbTe crystal.[36,37] Meanwhile, the hole mobility also decreased from 259 cm^2 V^{-1} s^{-1} to 226 cm^2 V^{-1} s^{-1} with increasing POM content (Fig. 4b), which is attributable to the enhanced carrier scattering at the interfacial oxide layers. Also, the intrinsically low electrical properties of the oxide phase can further reduce the hole concentration and mobility.

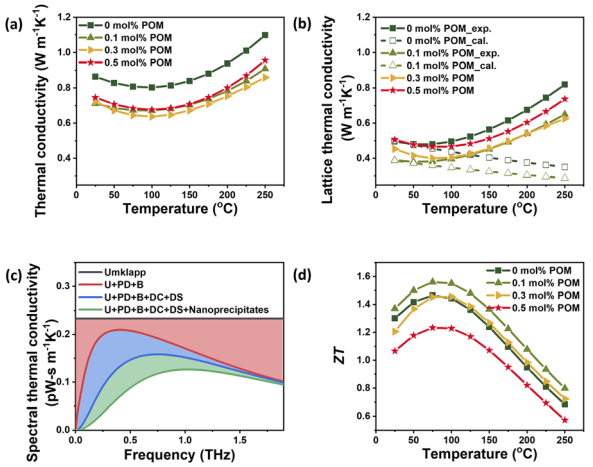

Fig. 5 Thermal properties of POM-coated BiSbTe. Temperature-dependent (a) thermal conductivity, (b) measured (solid) and fitted (dashed) lattice thermal conductivity of POM-coated BiSbTe samples. (c) Frequency-dependent spectral thermal conductivity of the 0.1 mol% POM-coated BiSbTe. (d) Temperature-dependence of figure of merit, *ZT*. (f) Comparison of ZT_{max} values of our 0.1 mol% POM-coated BiSbTe with those of recently reported BiSbTe materials. Detailed data are provided in Table S3.

Owing to the reduction of both hole mobility and concentration, the electrical conductivity decreases from 751 S cm^{-1} to 493 S cm^{-1} with increasing POM content at room temperature

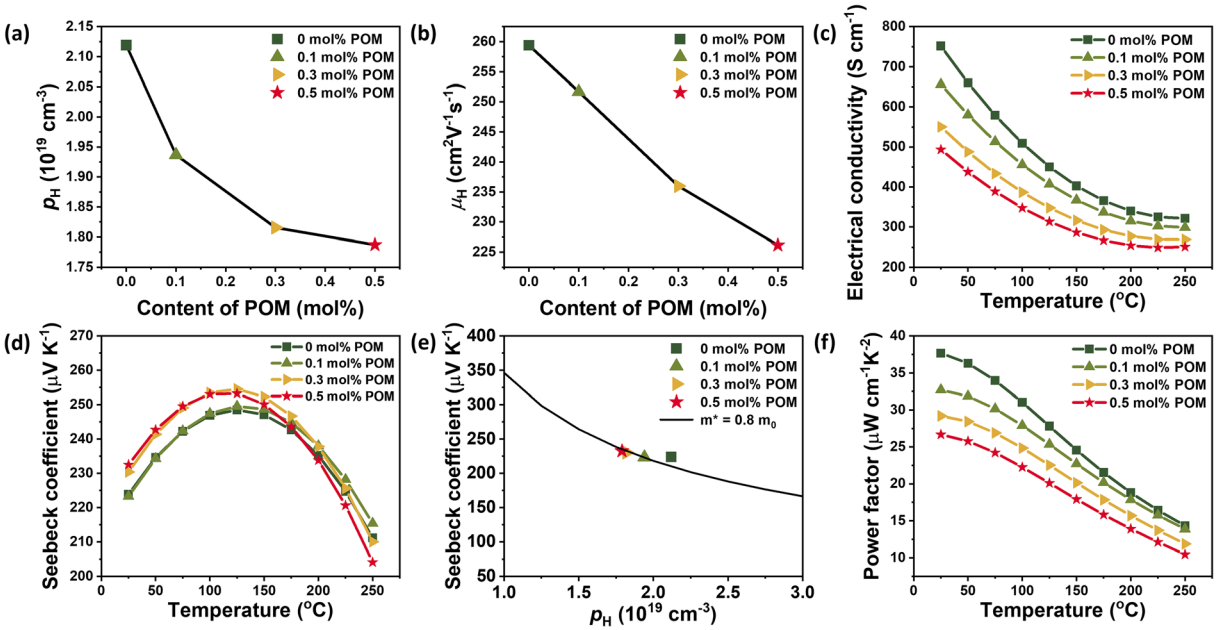

Fig. 4 Electrical properties of POM-coated BiSbTe. (a) Hole concentration and (b) mobility of POM-coated BiSbTe at room temperature. Temperature-dependent (c) electrical conductivity and (d) Seebeck coefficient with POM contents. (e) The Pisarenko plot of POM-coated BiSbTe at room temperature and the solid curve indicates the theoretical Seebeck coefficient *versus* the carrier concentration with an effective mass of $m^* = 0.8\ m_0$. (f) Temperature-dependent power factor with varying POM contents.

(Fig. 4c). As well, the electrical conductivity decreased with increasing temperature, characteristic of degenerate semiconductors. Accompanying the reduction in hole concentration, the Seebeck coefficient increases with increasing POM content (Fig. 4d) since the Seebeck coefficient is inversely proportional to the carrier concentration. At room temperature, the Seebeck coefficient rises slightly from 223.9 μV K^{-1} for the 0 mol% sample to 232.5 μV K^{-1} for the 0.5 mol% sample. All samples exhibited a peak value at 125 °C. Meanwhile, at high temperatures, the Seebeck coefficients of the samples with higher POM content decreased more swiftly. This result may come from the enhanced bipolar contribution to the samples with higher POM content since they have lower hole concentrations. The thermally excited minority carrier of electrons at high temperatures can more negatively affect the Seebeck coefficient in samples with lower hole concentrations.

To further clarify the influence of POM on the Seebeck coefficient, the effective mass (m^*) was estimated to use the single parabolic band (SPB) model (Fig. 4e), assuming negligible minority-carrier contribution. Although effective mass shows a slight downward trend with POM addition (Table S1) the stronger decrease in hole carrier concentration (p) dominates the $p^{-2/3}$ term, yielding a net increase in Seebeck coefficient over relevant temperature windows. In other words, the decline rate in effective mass is slower than that in hole carrier concentration, leading overall to an enhanced Seebeck coefficient. Although the Seebeck coefficient slightly increases with increasing POM content, the power factor decreases from 37.7 μW cm^{-1} K^{-2} to 26.7 μW cm^{-1} K^{-2} at room temperature due to the reduction in electrical conductivity (Fig. 4f).

The thermal conductivity exhibited a remarkable reduction in the POM-added samples. At room temperature, the pristine sample has a thermal conductivity of 0.86 W m^{-1} K^{-1}, while all samples with the POM exhibited values ranging from 0.71 to 0.74 W m^{-1} K^{-1} (Fig. 5a), suggesting phonon scattering at the oxide interfaces and induced dislocations. Further, the lattice thermal conductivity was calculated by subtracting the electronic thermal conductivity from the total thermal conductivity using the Wiedemann–Franz relation. Lattice heat transport accounts for more than 50% of total thermal conductivity in certain parts of the measured range (Fig. 5b), underscoring the importance of phonon scattering. The lattice thermal conductivity of pristine BiSbTe was 0.49 W m^{-1} K^{-1} at room temperature. This value is significantly lower than the reported values of polycrystalline BiSbTe[38–40] and similar to those of melt-spun and SPS BiSbTe.[41,42] Like the total thermal conductivity, all samples with the POM exhibited lower lattice thermal conductivity. The sample with 0.1 mol% of POM achieved a minimum value of 0.38 W m^{-1} K^{-1}, close to the Einstein limit of 0.3 W m^{-1} K^{-1}.[43] The significant reduction in thermal conductivity is attributed to phonon scattering across multiple length scales at the interfacial oxides and dislocations indued from the POM and nanostructures generated from the melt-spun BiSbTe. The multiscale phonon scattering leverages a combination of structural features at different length scales to maximize phonon scattering throughout the entire spectrum of heat-carrying vibrations.

The quantitative evidence supporting multiscale phonon scattering is provided through temperature-dependent lattice thermal conductivity fitting and frequency-dependent spectral thermal conductivity analysis (Table S2). As shown in Fig. 5b, the lattice thermal conductivity of the POM 0.1 mol% sample was reproduced using a Debye–Callaway model incorporating multiple phonon scattering processes, including Umklapp, point defect, grain boundary, dislocation, and nanoprecipitate scattering terms. The model shows excellent agreement with experimental data near room temperature, while lattice thermal conductivity at temperatures above 300 K was estimated *via* extrapolation based on the lattice thermal conductivity value at 298 K and its temperature dependence. The discrepancy between measured and calculated values at high temperatures is attributed to the contribution of bipolar conduction.

Furthermore, the frequency-dependent spectral thermal conductivity analysis in Fig. 5c semi-quantitatively resolves the contribution of each scattering mechanism across phonon frequencies. Grain boundary and point defect scattering effectively suppress phonons in both low- and high-frequency regimes, dislocation scattering dominates in the mid-frequency range, and nanoprecipitate scattering is most effective in the mid-to-high frequency regime. Thus, the combination of model-based fitting and spectral phonon analysis provides robust semi-quantitative evidence for multiscale phonon scattering spanning multiple phonon wavelength regimes in this composite system.

Interestingly, as the POM content increased, the lattice thermal conductivity at room temperature increased. This increasing tendency with increasing interfacial layer content agrees with a previous report[44] in which oxide interfacial layers were introduced into BiSbTe grains by the atomic layer deposition method. When the oxide second phase is thick enough to contribute to total thermal transport rather than the phonon scattering sites, the relatively higher thermal conductivity of oxides should contribute to lattice thermal conductivity of the composite samples and eventually enhance the total thermal conductivity. In the current study, the oxide phase created from the thermal decomposition of the POM is expected to be H_x-MoP_yO_z. Although, to the best of our knowledge, the thermal conductivity of these phases has not been reported in the literature, the reported values of the molybdenum oxides or phosphorus oxide phases range from a few to several hundred W m^{-1} K^{-1}.[45] Thus, we may speculate that the increased lattice thermal conductivity with increasing POM content is attributed to the contribution of the interfacial oxide layers.

The significant reduction of thermal conductivity enhanced the ZT values (Fig. 5d). The sample without POM addition exhibited a peak ZT of 1.46 at 75 °C, which lies within the range reported for high-performance BiSbTe synthesized from melt-spun powders.[30,46,47] The sample with POM 0.1 mol% achieved the highest ZT of 1.37 at room temperature and 1.56 at 75 °C, representing a 5.4–17% enhancement over pristine BST in the entire temperature range. This maximum value is comparable to or higher than those reported recently for BiSbTe (Table S3). The samples with higher POM content exhibited lower ZT values than the pristine sample due to the relatively lower power

factors and higher thermal conductivities, pointing out the importance of the optimum content of oxide layers. As a trade-off exists between lattice thermal conductivity reduction and charge transport degradation with increasing oxide content, optimizing the oxide content to maximize the overall *ZT* is crucial. These results demonstrate the effectiveness of the POM additive for phonon scattering and the enhancement of TE properties.

To further confirm the thermal stability of the POM-added samples, we repeated the thermoelectric property measurements three times under a He atmosphere up to 250 °C (Fig. S14). The results showed excellent reproducibility with relative errors of 0.2–6%. This reproducibility suggests that no noticeable degradation occurs during repeated thermal cycling under the tested conditions.

Conclusion

In summary, we have developed hierarchical phonon-engineered BiSbTe materials by integrating POM-induced interfacial oxide layers with melt-spun nanostructuring. Through melt spinning and subsequent POM coating followed by spark plasma sintering, multiscale structural features were introduced, including nanostructures and oxide interfacial layers, as well as wide range of grain sizes. As a result, the lattice thermal conductivity was markedly reduced to 0.38 W m^{-1} K^{-1} at room temperature for the 0.1 mol% POM sample, representing an ~20% decrease relative to pristine BiSbTe. Thus, this sample achieved a maximum *ZT* value of 1.56 at 75 °C. Distinct from conventional melt-spun BiSbTe studies, our approach employs a scalable, solution-based oxide coating strategy that allows precise and independent control of interfacial structures without relying on melt-spinning parameter optimization. Moreover, this work demonstrates the role of POMs as multi-functional molecular additives that simultaneously enhance phonon scattering and interfacial controllability, while offering a compositionally versatile platform for designing high-*ZT* thermoelectric materials through molecular-level interface engineering.

Author contributions

Yae Eun Park: conceptualization, data curation, formal analysis, investigation, methodology, and writing – original draft. Hyunjin Han: conceptualization, data curation, formal analysis, investigation, methodology, and writing – original draft. Sung-Jin Jung: conceptualization, data curation, formal analysis, funding acquisition, and writing – review & editing. Junwoo Song: data curation, formal analysis. Jino Kim: data curation, formal analysis. Jungwon Na: investigation, formal analysis. Kwangjoo Kim: data curation, formal analysis. Insub Lee: data curation, formal analysis. Hoon Wee: data curation, formal analysis, funding acquisition. Joonhyun Lee: data curation, formal analysis, funding acquisition. Sungjun Yang: methodology and writing. Seungki Jo: methodology and writing. Ho Seong Lee: methodology and writing – review & editing. Tae Joo Shin: methodology and writing. Youngdeog Koh: data curation, and writing – review & editing. Jae Sung Son: conceptualization, supervision, funding acquisition, writing – original draft, and writing – review & editing.

Conflicts of interest

There are no conflicts to declare.

Data availability

Data are available upon request from the authors. Supplementary information (SI): additional experimental details and figures and tables. See DOI: https://doi.org/10.1039/D5TA09730D.

Acknowledgements

This research was supported by the National Research Foundation of Korea (NRF) funded by the Ministry of Science, ICT (RS-2024-00449743 and 2022M3H4A1A04076667).

References

1 L. E. Bell, *Science*, 2008, **321**, 1457–1461.
2 F. J. DiSalvo, *Science*, 1999, **285**, 703–706.
3 J. He and T. M. Tritt, *Science*, 2017, **357**, eaak9997.
4 A. Shakouri, *Annu. Rev. Mater. Res.*, 2011, **41**, 399–431.
5 G. J. Snyder and E. S. Toberer, *Nat. Mater.*, 2008, **7**, 105–114.
6 M. Zebarjadi, K. Esfarjani, M. Dresselhaus, Z. Ren and G. Chen, *Energy Environ. Sci.*, 2012, **5**, 5147–5162.
7 P. Jood, R. J. Mehta, Y. Zhang, T. Borca-Tasciuc, S. X. Dou, D. J. Singh and G. Ramanath, *RSC Adv.*, 2014, **4**, 6363–6368.
8 B. Peng, H. Mei, H. Zhang, H. Shao, K. Xu, G. Ni, Q. Jin, C. M. Soukoulis and H. Zhu, *Inorg. Chem. Front.*, 2019, **6**, 920–928.
9 Z. Li, H. Xie, Y. Xia, S. Hao, K. Pal, M. G. Kanatzidis, C. Wolverton and X. Tang, *Chem. Mater.*, 2022, **34**, 1289–1301.
10 W. Li, S. Lin, B. Ge, J. Yang, W. Zhang and Y. Pei, *Adv. Sci.*, 2016, **3**, 1600196.
11 L. D. Zhao, S. H. Lo, Y. Zhang, H. Sun, G. Tan, C. Uher, C. Wolverton, V. P. Dravid and M. G. Kanatzidis, *Nature*, 2014, **508**, 373–377.
12 O. Delaire, J. Ma, K. Marty, A. F. May, M. A. McGuire, M.-H. Du, D. J. Singh, A. Podlesnyak, G. Ehlers and M. Lumsden, *Nat. Mater.*, 2011, **10**, 614–619.
13 S. R. Brown, S. M. Kauzlarich, F. Gascoin and G. J. Snyder, *Chem. Mater.*, 2006, **18**, 1873–1877.
14 Y. Pei, X. Shi, A. LaLonde, H. Wang, L. Chen and G. J. Snyder, *Nature*, 2011, **473**, 66–69.
15 J. Zhang, L. Song, S. H. Pedersen, H. Yin, L. T. Hung and B. B. Iversen, *Nat. Commun.*, 2017, **8**, 13901.
16 S. Jo, S. H. Park, H. W. Ban, D. H. Gu, B.-S. Kim, J. H. Son, H.-K. Hong, Z. Lee, H.-S. Han and W. Jo, *J. Alloys Compd.*, 2016, **689**, 899–907.
17 M. G. Kanatzidis, *Chem. Mater.*, 2010, **22**, 648–659.

18 P. F. Poudeu, J. D'Angelo, A. D. Downey, J. L. Short, T. P. Hogan and M. G. Kanatzidis, *Angew. Chem., Int. Ed.*, 2006, **45**, 3835–3839.
19 K. Biswas, J. He, I. D. Blum, C.-I. Wu, T. P. Hogan, D. N. Seidman, V. P. Dravid and M. G. Kanatzidis, *Nature*, 2012, **489**, 414–418.
20 B. Qin, Y. Zhang, D. Wang, Q. Zhao, B. Gu, H. Wu, H. Zhang, B. Ye, S. J. Pennycook and L.-D. Zhao, *J. Am. Chem. Soc.*, 2020, **142**, 5901–5909.
21 Y. Jiang, J. Dong, H.-L. Zhuang, J. Yu, B. Su, H. Li, J. Pei, F.-H. Sun, M. Zhou, H. Hu, J.-W. Li, Z. Han, B.-P. Zhang, T. Mori and J.-F. Li, *Nat. Commun.*, 2022, **13**, 6087.
22 Z. Chen, X. Zhang and Y. Pei, *Adv. Mater.*, 2018, **30**, 1705617.
23 T. Hori and J. Shiomi, *Sci. Technol. Adv. Mater.*, 2019, **20**, 10–25.
24 A. Le Bail, *Powder Diffr.*, 2005, **20**, 316–326.
25 M. Fournier, A. Aouissi and C. Rocchiccioli-Deltcheff, *J. Chem. Soc., Chem. Commun.*, 1994, 307–308.
26 S. Ilhan, C. Kahruman and I. Yusufoglu, *J. Anal. Appl. Pyrolysis*, 2007, **78**, 363–370.
27 I. Koshiishi and T. Imanari, *J. Chromatogr. A*, 1986, **358**, 195–200.
28 S. I. Wright and M. M. Nowell, *Microsc. Microanal.*, 2006, **12**, 72–84.
29 M. Kim and H. S. Park, *Appl. Microsc.*, 2022, **52**, 2.
30 W. Xie, X. Tang, Y. Yan, Q. Zhang and T. M. Tritt, *Appl. Phys. Lett.*, 2009, **94**, 102111.
31 S. I. Kim, K. H. Lee, H. A. Mun, H. S. Kim, S. W. Hwang, J. W. Roh, D. J. Yang, W. H. Shin, X. S. Li, Y. H. Lee, G. J. Snyder and S. W. Kim, *Science*, 2015, **348**, 109–114.
32 D. Hull and D. J. Bacon, *Introduction to Dislocations*, Elsevier, 2011.
33 L. Dong, J. Schnitker, R. W. Smith and D. J. Srolovitz, *J. Appl. Phys.*, 1998, **83**, 217–227.
34 S. Ryu, K. Kang and W. Cai, *J. Mater. Res.*, 2011, **26**, 2335–2354.
35 D. L. Medlin, N. Yang, C. D. Spataru, L. M. Hale and Y. Mishin, *Nat. Commun.*, 2019, **10**, 1820.
36 L.-P. Hu, T.-J. Zhu, Y.-G. Wang, H.-H. Xie, Z.-J. Xu and X.-B. Zhao, *NPG Asia Mater.*, 2014, **6**, e88.
37 Y. Li, M. Ren, Z. Sun and Z. Yao, *RSC Adv.*, 2021, **11**, 36636–36643.
38 B. Poudel, Q. Hao, Y. Ma, Y. Lan, A. Minnich, B. Yu, X. Yan, D. Wang, A. Muto and D. Vashaee, *Science*, 2008, **320**, 634–638.
39 E. Symeou, C. Nicolaou, A. Delimitis, J. Androulakis, T. Kyratsi and J. Giapintzakis, *J. Solid State Chem.*, 2019, **270**, 388–397.
40 Y. Zheng, Q. Zhang, X. Su, H. Xie, S. Shu, T. Chen, G. Tan, Y. Yan, X. Tang and C. Uher, *Adv. Energy Mater.*, 2015, **5**, 1401391.
41 W. H. Shin, J. S. Yoon, M. Jeong, J. M. Song, S. Kim, J. W. Roh, S. Lee, W. S. Seo, S. W. Kim and K. H. Lee, *Crystals*, 2017, **7**, 180.
42 Y. Zheng, G. Tan, Y. Luo, X. Su, Y. Yan and X. Tang, *Materials*, 2017, **10**, 617.
43 R. Prasher, *Phys. Rev. B: Condens. Matter*, 2006, **74**, 165413.
44 S. Lee, G. M. Park, Y. Kim, S.-H. Lee, S.-J. Jung, J. Hong, S.-C. Kim, S. O. Won, A. S. Lee, Y. J. Chung, J.-Y. Kim, H. Kim, S.-H. Baek, J.-S. Kim, T. J. Park and S. K. Kim, *ACS Appl. Mater. Interfaces*, 2024, **16**, 17683–17691.
45 A. Turnbull, *J. Chem. Eng. Data*, 1965, **10**, 118–119.
46 W. Xie, J. He, H. J. Kang, X. Tang, S. Zhu, M. Laver, S. Wang, J. R. D. Copley, C. M. Brown, Q. Zhang and T. M. Tritt, *Nano Lett.*, 2010, **10**, 3283–3289.
47 L. Han, S. H. Spangsdorf, N. V. Nong, L. T. Hung, Y. B. Zhang, H. N. Pham, Y. Z. Chen, A. Roch, L. Stepien and N. Pryds, *RSC Adv.*, 2016, **6**, 59565.

